AGU PUBLICATIONS

Geophysical Research Letters

RESEARCH LETTER
10.1002/2017GL072830

Key Points:
- MMS observations of the fine structure of the reconnection exhaust region close to an X line
- The parallel crescent distributions and associated field signatures suggest MMS passage through the outer EDR downstream of an X line
- Near the magnetospheric separatrix large-amplitude electric fields including field-aligned components accelerate electrons toward the X line

Correspondence to:
K.-J. Hwang,
kyoung-joo.hwang@nasa.gov

Citation:
Hwang, K.-J., et al. (2017), Magnetospheric Multiscale mission observations of the outer electron diffusion region, *Geophys. Res. Lett.*, *44*, 2049–2059, doi:10.1002/2017GL072830.

Received 26 JAN 2017
Accepted 13 FEB 2017
Accepted article online 15 FEB 2017
Published online 2 MAR 2017

Magnetospheric Multiscale mission observations of the outer electron diffusion region

K.-J. Hwang[1,2], D. G. Sibeck[1], E. Choi[1,3], L.-J. Chen[1,2], R. E. Ergun[4], Y. Khotyaintsev[5], B. L. Giles[1], C. J. Pollock[6], D. Gershman[1], J. C. Dorelli[1], L. Avanov[1], W. R. Paterson[1], J. L. Burch[7], C. T. Russell[8], R. J. Strangeway[8], and R. B. Torbert[9]

[1]NASA Goddard Space Flight Center, Greenbelt, Maryland, USA, [2]The Goddard Planetary Heliophysics Institute, University of Maryland, Baltimore, Maryland, USA, [3]Center for Research and Exploration in Space Science and Technology, Universities Space Research Association, Greenbelt, Maryland, USA, [4]Laboratory for Atmospheric and Space Physics, University of Colorado at Boulder, Boulder, Colorado, USA, [5]Swedish Institute of Space Physics, Uppsala, Sweden, [6]Denali Scientific, LLC, Healy, Alaska, [7]Southwest Research Institute, San Antonio, Texas, USA, [8]Institute of Geophysics and Planetary Physics, University of California, Los Angeles, California, USA, [9]Space Science Center, University of New Hampshire, Durham, New Hampshire, USA

Abstract This paper presents Magnetospheric Multiscale mission (MMS) observations of the exhaust region in the vicinity of the central reconnection site in Earth's magnetopause current sheet. High-time-resolution measurements of field and particle distributions enable us to explore the fine structure of the diffusion region near the X line. Ions are decoupled from the magnetic field throughout the entire current sheet crossing. Electron jets flow downstream from the X line at speeds greater than the $\mathbf{E}\times\mathbf{B}$ drift velocity. At/around the magnetospheric separatrix, large-amplitude electric fields containing field-aligned components accelerate electrons along the magnetic field toward the X line. Near the neutral sheet, crescent-shaped electron distributions appear coincident with (1) an out-of-plane electric field whose polarity is opposite to that of the reconnection electric field and (2) the energy transfer from bulk kinetic to field energy. The observations indicate that MMS passed through the edge of an elongated electron diffusion region (EDR) or the outer EDR in the exhaust region.

1. Introduction

Earth's magnetopause hosts a number of instabilities that mediate the entry of solar wind mass, energy, and momentum into the magnetosphere. Magnetic reconnection, one of the major solar wind-magnetosphere coupling mechanisms, enables plasmas populating the reconnecting magnetic fields to intermix and converts large amounts of magnetic energy into kinetic energy.

The multiscale physics of reconnection has long been a topic for attention in the space and laboratory plasma discipline: reconnection has large-scale effects such as influences on the energy budget of the entire magnetosphere, plasma transport, and the dynamics of mesoscale to macroscale plasma structures, e.g., in conjunction with the generation of flux transfer events and dipolarization fronts and their global propagation. The initiation and reconfiguration of magnetic topologies associated with reconnection are thought to arise in the electron diffusion region (EDR) where electrons are demagnetized. This region is embedded within a much larger ion diffusion region (IDR) where Hall physics resulting from demagnetized ions governs the magnetofluid description. Although the observation of IDRs has been facilitated by their magnetic and electric field geometry, the EDR is difficult to identify mainly due to its small size in conjunction with the limited time resolution of plasma measurements.

Important reconnection parameters such as the reconnection rate are thought to be controlled by microphysical processes occurring at these EDR/IDR scales. Yet the topology and electron physics of, in particular, the EDR has been the subject of prolific controversy. Previous numerical studies by *Hesse et al.* [1999], *Shay et al.* [2001], *Birn et al.* [2001], *Rogers et al.* [2001], and *Ricci et al.* [2002] concur that EDR dynamics plays an insignificant role in regulating the efficiency of reconnection as the process evolves into the quasi-steady realm. In these models, the EDR and the IDR extend a few to several d_e (electron inertial lengths) and ~10 d_i (ion inertial lengths), respectively, in the outflow direction.

By contrast, recent endeavors to resolve the structure of the EDR [*Daughton et al.*, 2006; *Fujimoto*, 2006; *Karimabadi et al.*, 2007; *Shay et al.*, 2007; *Zenitani et al.*, 2011] suggested that the EDR is not localized but extends tens of d_i along the exhaust regions. Furthermore, they proposed that the EDR consists of inner and outer regions and that the inner region regulates the reconnection rate. The inner region containing the X line features a strong electron current into/out of the reconnection plane and a dissipative electric field (nonzero $\mathbf{E}' = \mathbf{E} + \mathbf{V}_e \times \mathbf{B}$ and electrons lagging the magnetic field, i.e., $\mathbf{J} \cdot \mathbf{E}' > 0$). The outer region is characterized by highly collimated electron jets that outrun the moving magnetic field, leading to the out-of-plane (m-directional) component of E' having an opposite sign to the inner-region $E_m^{'}$ and $\mathbf{J} \cdot \mathbf{E}' < 0$. *Karimabadi et al.* [2007] showed that the electron bulk flow slows down in the outer region, converting the bulk kinetic energy to thermal energy.

Recent theoretical and modeling efforts described the ion and electron behavior and resulting particle distributions in different boundary layers and parameter regimes of both antiparallel and guide-field reconnection [e.g., *Egedal et al.*, 2012; *Hesse et al.*, 2014; *Bessho et al.*, 2014; *Shuster et al.*, 2015]. For example, electrons develop agyrotropic distribution functions as a result of the coexistence of high velocity particles emerging from the EDR and low-velocity populations entering it [*Hesse*, 2006]. The electron distribution function exhibits striated and triangular structures near the X line due to particle reflections, but in the EDR downstream from the X line electron outflow jets with swirls, arcs, and rings [*Shuster et al.*, 2015]. Meandering particle motion in oppositely directed magnetic fields forms a crescent-shaped distribution function [*Hesse et al.*, 2014; *Chen et al.*, 2016].

The crescent-shape electron distributions expected near the central neutral sheet have recently been seen in in situ observations from the Magnetospheric Multiscale mission (MMS) [*Burch et al.*, 2016]. Launched in March 2015, MMS provides unprecedented time-resolution measurements of particles and fields, enabling more precise mapping of kinetic boundaries in reconnection regions and quantitative testing of the microscale and mesoscale physics predicted by modeling efforts [e.g., *Eriksson et al.*, 2016; *Khotyaintsev et al.*, 2016; *Norgren et al.*, 2016].

In this paper, we make full use of MMS observations on 19 September 2015 that indicate a crossing of the outer EDR region to resolve and understand reconnection processes occurring at the edge of the elongated EDR. We compare these observations with results from a kinetic PIC simulation of asymmetric reconnection performed by *Chen et al.* [2016]. In the following section we briefly describe the MMS instruments used for the present study. We present an overview of the event and reconnection geometry indicated from the data set in section 3 and show the detailed electron distribution functions, the current density, the dissipative electric field, and the corresponding energy budget in section 4. Discussion and conclusions follow in section 5.

2. Instrumentation

The four MMS spacecraft [*Burch et al.*, 2015] fly in highly elliptical equatorial orbits with perigee at 1.2 Earth radii (R_E) and apogee at 12 R_E. The spacecraft are identically equipped with instruments including fast plasma investigations (FPI) [*Pollock et al.*, 2016], fluxgate magnetometers (FGM consisting of the digital fluxgate magnetometer (DFG) and the analogue fluxgate magnetometer (AFG)) [*Russell et al.*, 2014], and electric field instruments consisting of the spin-plane double probe (SDP) [*Lindqvist et al.*, 2016] and the axial double probe (ADP) [*Ergun et al.*, 2014]. We used the magnetic field data from FGM with a time resolution of 10 ms in burst mode, the DC electric field data calibrated from SDP and ADP (with a 1 ms time resolution in burst mode), and particle data from the Fast Plasma Investigation (FPI) with 150 ms (FPI-DIS data for ions) and 30 ms (FPI-DES data for electrons) time resolution in burst mode.

3. Reconnection Geometry

At ~0910:00 UT on 19 September 2015, the barycenter of the MMS quartet was located at the postnoon magnetopause south of the magnetic equator, at [6.4, 6.5, −4.1] R_E in Geocentric Solar Magnetospheric (GSM) coordinates. Figures 1 and 2 show the detailed field and particle signatures from 0909:56.4 to 0909:59.3 UT observed by MMS3 (Figure 1) and from 0909:56.7 to 0909:59.9 UT observed by MMS4 (Figure 2), respectively. MMS3 and MMS4 are separated predominantly along X_{GSM} direction by ~65.4 km ($X_{\mathrm{MMS3}} > X_{\mathrm{MMS4}}$). Figures 1a and 2a present the magnetic strength (black profiles) together with the magnetic field components in the LMN boundary coordinate system: B_l (red), B_m (green), and B_n (blue). We determined the LMN coordinates by employing minimum variance analysis (MVA) [*Sonnerup and Scheible*, 1998] using the

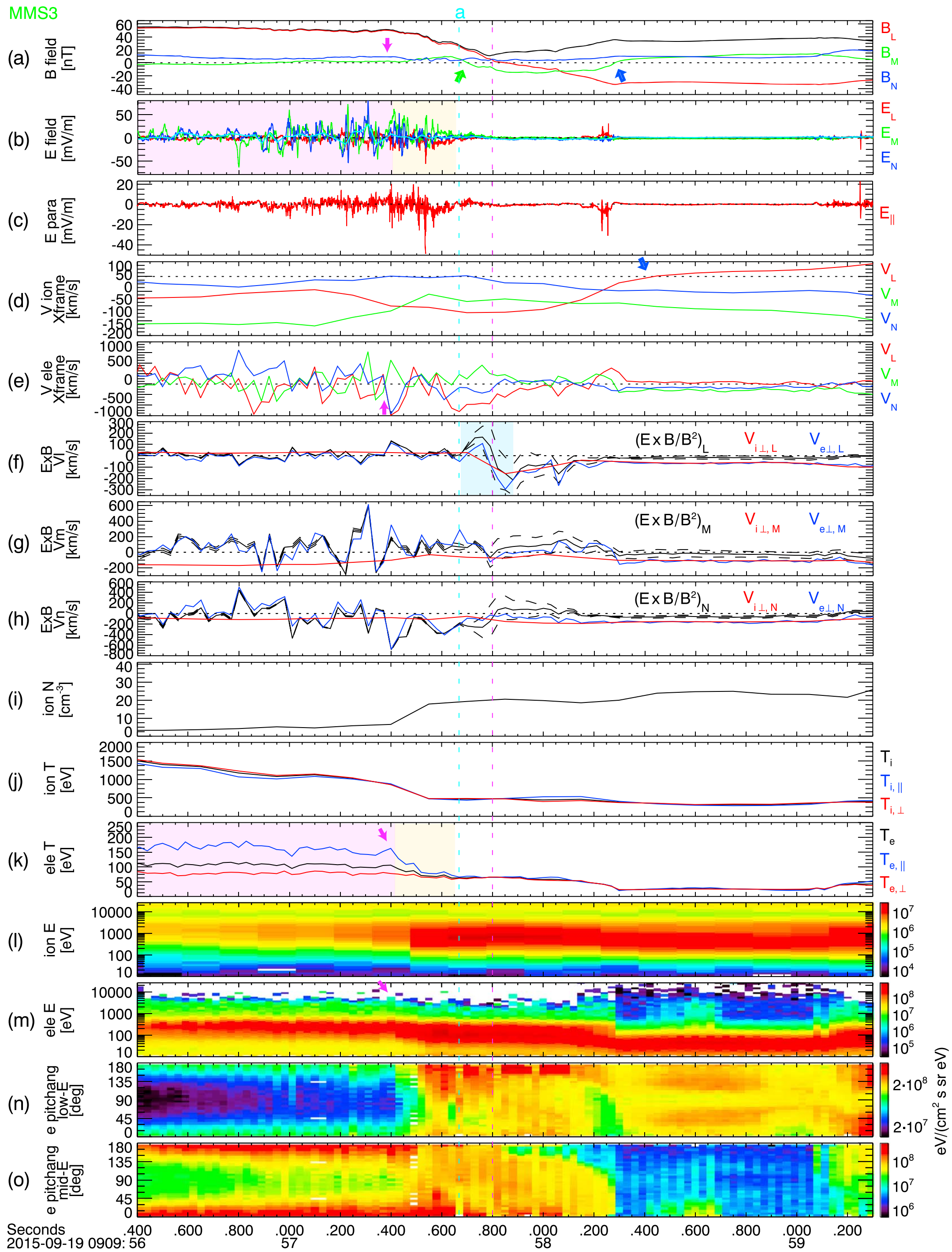

Figure 1. Overview of the magnetopause current sheet crossing by MMS3: (a) The magnetic field in LMN; (b) the electric field in LMN; (c) the DC parallel electric field; (d) the ion and (e) electron bulk velocity in the moving current sheet frame; (f–h) the l, m, n components of $\mathbf{E} \times \mathbf{B}$ drift velocity (black profiles) superposed with the ion (red) and electron (blue) perpendicular velocities; (i) the ion number density; (j) the ion/(k) electron total (black), parallel (blue), and perpendicular (red) temperatures; the (l) ion and (m) electron energy spectrogram; the pitch angle distribution of the (n) low-energy (<100 eV) and (o) midenergy (100 eV < energy < 1 keV) electrons. The vertical magenta (cyan) dashed line indicates the neutral sheet (the time selected for the electron distributions is shown in Figure 3Ca).

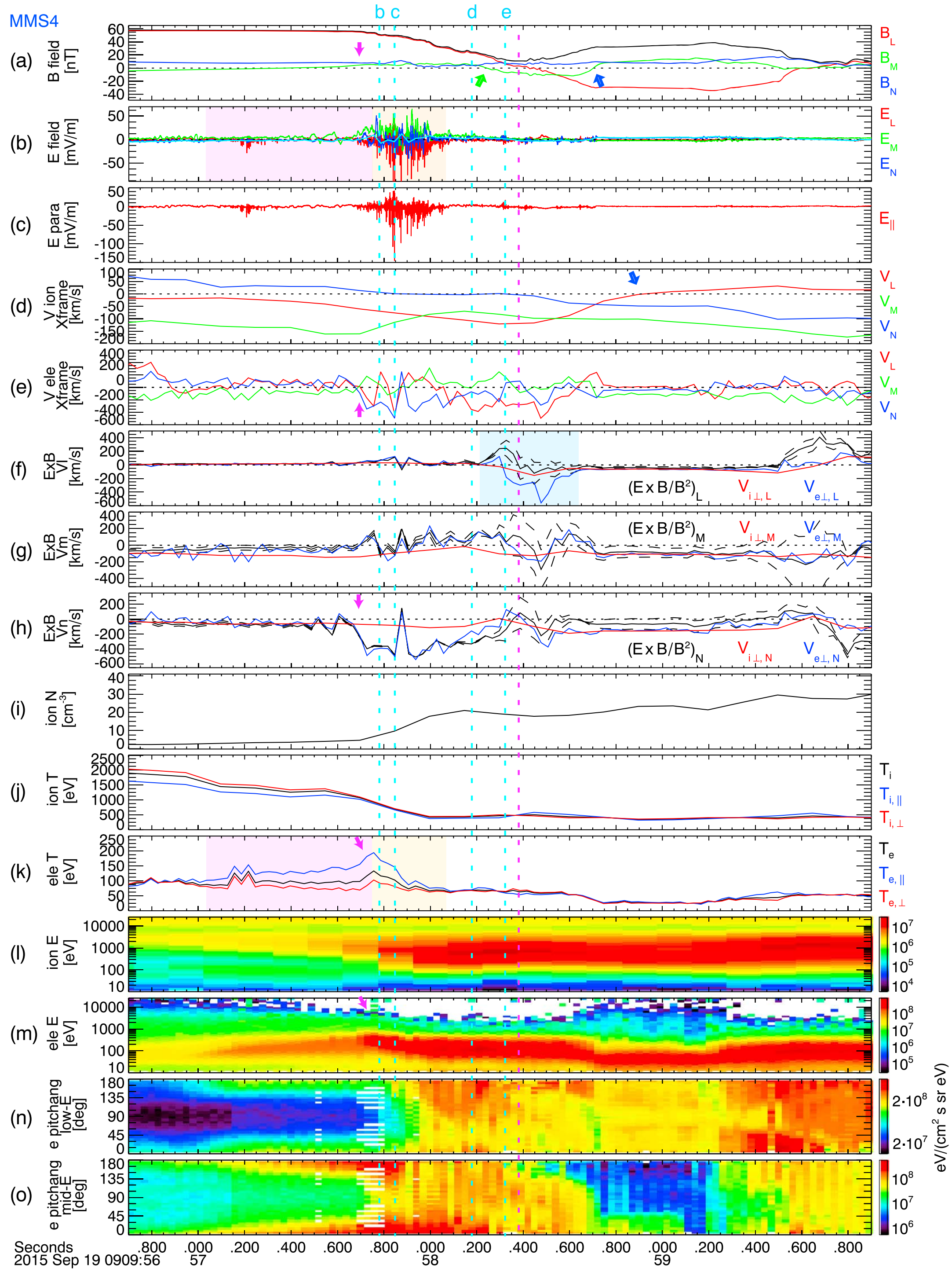

Figure 2. The magnetopause current sheet crossing by MMS4. Same format as Figure 1. The vertical magenta (cyan) dashed line indicates the neutral sheet (the times selected for the electron distributions are shown in Figures 3Cb–3Ce).

magnetic field data obtained from MMS2 for the period between ~0909:57 and 0909:59 UT around the current sheet crossing indicated by the B_z reversal across the vertical magenta dashed line in Figures 1 and 2: **l** = [−0.09, 0.67, 0.74], **m** = [0.01, −0.74, 0.67], **n** = [0.99, 0.07, 0.06] (The MVA using magnetic field data from other spacecraft gives almost identical LMN coordinates). The medium-to-minimum (maximum-to-medium) eigenvalue ratio is ~12 (16), indicating a reliable calculation [*Lepping and Behannon*, 1980]. To

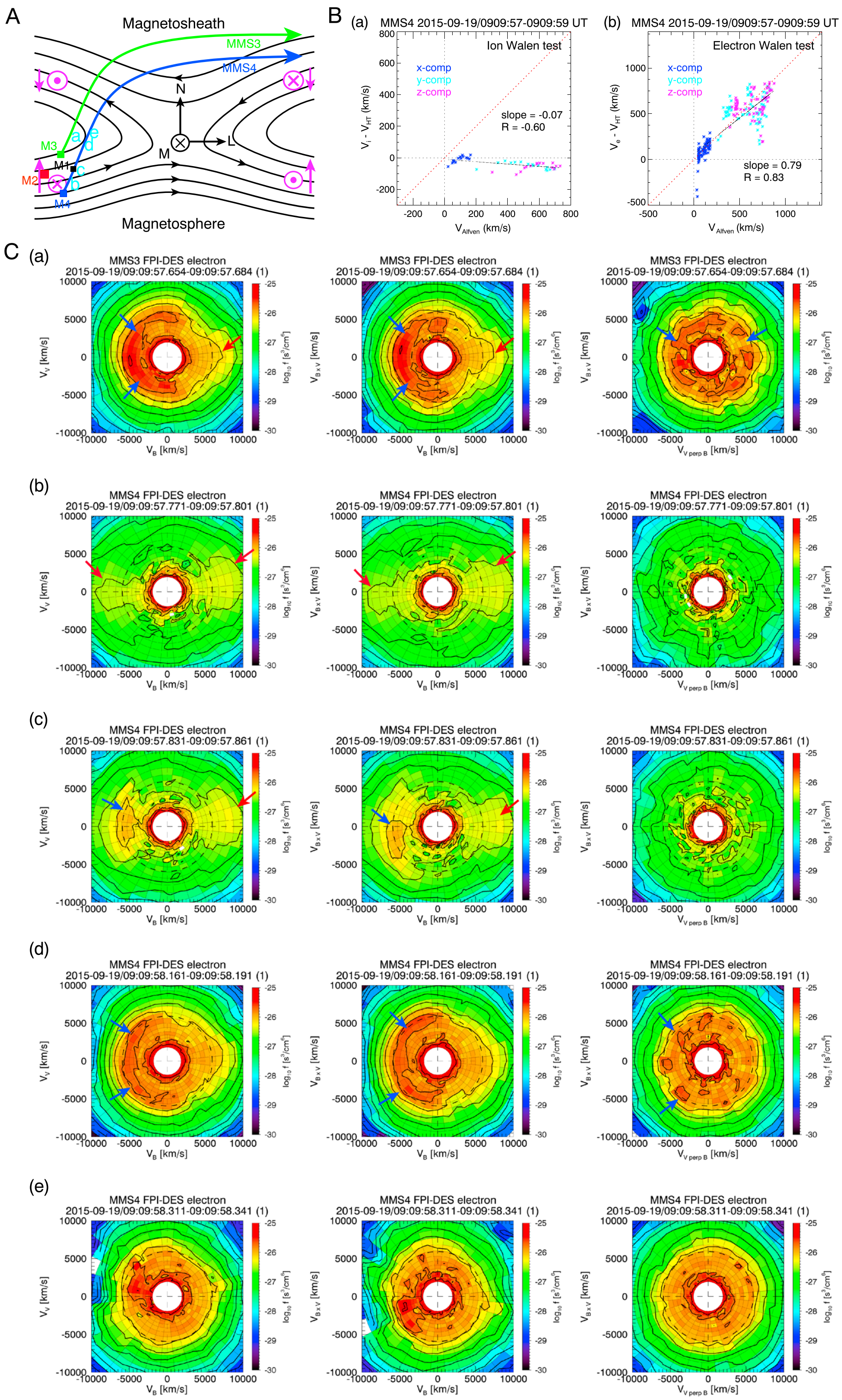

Figure 3. (A) An illustration of the relative spacecraft trajectory in the vicinity of the reconnection X line. The distance (x) of the spacecraft crossing the current sheet along/downstream of the X line is estimated to 1.5–2.5 d_i (the ion inertial length). (B) Ion (left) and electron (right) Walén tests for MMS4 passage of the current sheet. (C) Electron distributions measured by FPI-DES with a 30 ms time resolution at selected times, denoted by "a" to "f" in Figures 1, 2, and 3A. The left and middle column distributions are shown as a function of ($\mathbf{V}_{||}$, $\mathbf{V}_{\perp 1}$) and ($\mathbf{V}_{||}$, $\mathbf{V}_{\perp 2}$), respectively. Parallel and perpendicular directions are defined with respect to the local magnetic field (**B**). The two perpendicular directions are chosen to be perpendicular to **B** along the ion bulk velocity, **V** ($\perp$ 1) and $\mathbf{B} \times \mathbf{V}$ ($\perp$ 2). The right column shows the distribution as a function of ($\mathbf{V}_{\perp 1}$, $\mathbf{V}_{\perp 2}$). Each panel contains a dotted circle with a ~6.2×10^3 km/s radius that corresponds to an electron energy of 100 eV for better comparisons between distributions.

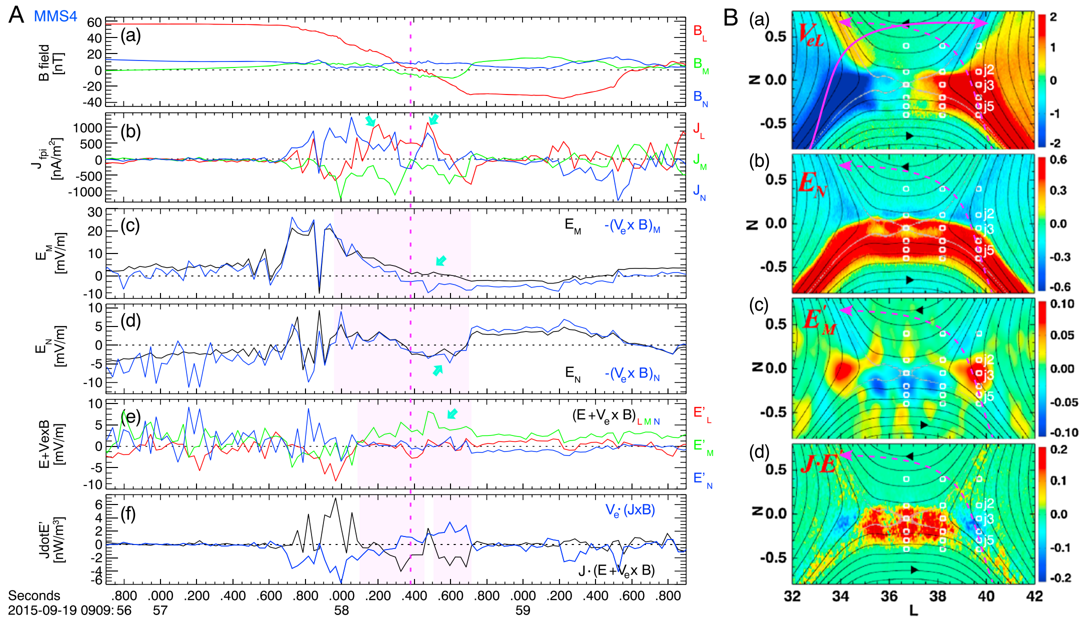

Figure 4. (A) MMS4 observations: (a) the magnetic field in LMN coordinates, (b) the current densities calculated from FPI plasma moments, (c, d) the E_m and E_n components: overplotted is the $-\mathbf{V_e} \times \mathbf{B}$ term (blue profiles), (e) the dissipative electric field or the electric field in the electron's rest frame, $\mathbf{E}' = \mathbf{E} + \mathbf{V}_e \times \mathbf{B}$, and (f) the Joule heating or the electron dissipation measure [*Zenitani et al*., 2011], $\mathbf{J} \cdot \mathbf{E}'$ (black): overplotted is $\mathbf{V}_e \cdot (\mathbf{J} \times \mathbf{B})$ indicating energy transfer between magnetic and bulk kinetic energy (blue). (B) Adopted from *Chen et al*. [2016]. Lines represent the model magnetic fields of the PIC simulation. Color coded are (a) the bulk electron velocity along *l*, (b) the current-sheet normal electric field, (c) the *m* component of $\mathbf{E}' = \mathbf{E} + \mathbf{V}_e \times \mathbf{B}$, and (d) $\mathbf{J} \cdot \mathbf{E}'$. A solid magenta line denotes an MMS trajectory speculated for the event. A dashed line starting on the other side of the X line is introduced for a better comparison between observation and simulation results.

comply with conventions, *m* points from postnoon to prenoon along the magnetopause, and *n* points outward from the magnetopause. All the parameters in Figures 1, 2, and 4 are shown in LMN coordinates.

Figures 1b and 2b show the electric field components. Figures 1, 2d, and 2e present the ion and electron velocity components in the rest frame of the moving current sheet. The four spacecraft with an average separation of ~63.8 km (MMS configurations indicated by black, red, green and blue rectangles in Figure 3A) were in a tetrahedron formation enabling us to determine the normal propagation velocity of the current sheet (indicative of the X line velocity) via timing analysis [*Paschmann and Daly*, 1998]: [−38.7, −4.9, −140.4] km/s in LMN ([−136.2, −31.9, −40.9] km/s in GSM). The bulk plasma velocities perpendicular to the magnetic field are compared with the $\mathbf{E} \times \mathbf{B}/B^2$ velocity in Figures 1 and 2f–2h. The ion number densities are presented in Figures 1i and 2i. Figures 1, 2j, and 2k show the ion and electron total (black profiles), parallel (blue), and perpendicular (red) temperatures. The color-coded ion (Figures 1l and 2l) and electron (Figures 1m and 2m) energy spectrograms, and the pitch angle distributions of the low-energy (<100 eV) and midenergy (100 eV < energy < 1 keV) electrons follow (Figures 1, 2n, and 2o, respectively).

The event occurred under dawnward (mainly) and southward interplanetary magnetic field conditions according to ACE observation (not shown). At MMS location ([6.4, 6.5, −4.1] R_E), the magnetosheath field is relatively antiparallel to the magnetopause magnetic field with a magnetic shear angle of ~153°. The event was embedded within a series of large-scale nonlinear Kelvin-Helmholtz waves as indicated by the repeated waveform whose steepness is larger at the leading edge than the trailing edge (not shown). The vortical motion of the Kelvin-Helmholtz waves can lead to thinning of the magnetopause current sheet, facilitating magnetic reconnection [e.g., *Otto and Fairfield*, 2000; *Nakamura et al*., 2006].

MMS traversed the current sheet from the magnetospheric side to the magnetosheath side, as inferred from the positive-to-negative B_z reversal across the magnetic strength minimum (Figures 1a and 2a), increasing densities (Figures 1i and 2i), decreasing temperatures (Figures 1, 2j, and 2k), and growing fluxes of magnetosheath ions and electrons with energies of less than a few keV and less than a few 100 eV, respectively

(Figures 1 and 2l–2o) over the event period. At ~0909:57.8/0909:58.4 UT at MMS3/MMS4 (the vertical magenta dashed lines in Figures 1 and 2), B_l changes sign while B_n has a finite positive value of ~5 nT (Figures 1a and 2a). About 0.15 s earlier, B_m shows weakly positive-to-negative changes (green arrows in Figures 1a and 2a). This bipolar B_m component represents a portion of the quadrupolar Hall magnetic field that is developed during reconnection due to the decoupling (coupling) of the ions (electrons) to the moving magnetic field within the IDR (see magenta symbols in Figure 3A). The Hall magnetic field for asymmetric magnetopause reconnection is often observed to be asymmetric [*Mozer et al*., 2008; *Lavraud et al*., 2016] or become bipolar [*Pritchett*, 2008].

At ~0909:57.4/0909:57.7 UT for MMS3/MMS4 (magenta arrows in Figures 1a, 1e, 1h, 1k, 1m, 2a, 2e, 2h, 2k, and 2m), B_l (B_m) begins to noticeably decrease (become positive); both $V_{e,n}$ and $V_{e,l}$ (bulk electron velocities to **l** and **n**) change from positive-to-negative (on average, in particular for MMS3), preceding large outflow jets near the current sheet; a local acceleration of electrons (mostly parallel to **B**) is seen. This boundary between the inflow and outflow electron jets, often called the electron edge, is located closely adjacent to the separatrix toward the current sheet [*Gosling et al*., 1990]. We delineate this location as the outer (toward the magnetosheath side) edge of the magnetospheric separatrix region.

The electric field is enhanced at and around the magnetospheric separatrix (magenta and yellow shades in Figures 1b and 2b). During the magenta-shade interval, E_m and E_n components that are mostly perpendicular to the local magnetic field (**B**) dominate E_l (~parallel to **B**) (Figure 1b) or either E_l or E_m dominates E_n (Figure 2b). During the yellow-shade interval corresponding to the crossing of the edge of the magnetospheric exhaust region, the large-amplitude electric fields are highly nonlinear (nonsinusoidal often in association with plasma structures such as electron phase-space holes and double layers). $E_{||}$ consists of a series of asymmetric (larger negative excursions than positive excursions), short-duration (~1 ms) spikes (Figures 1c and 2c). Considering the DC electric field uncertainty due to a cold plasma wake from the spacecraft [e.g., *Engwall et al*., 2006] (~5 mV/m in $E_{||}$ for the event), the DC $E_{||} \approx -7$ mV/m averaged over a ~30 ms period at 0909:57.53 UT (surrounding the -55 mV/m spike in Figure 1c) indicates a possible net negative $E_{||}$ (antiparallel electric field). The 30 ms averaged $E_{||}$ at 09:09:57.97 UT (just after the -145 mV/m excursion in $E_{||}$ in Figure 2c) is ~ -6 mV/m. Such parallel electric fields could result in electron beams in the positive **B** direction (section 4). In this event, the observations allow for a net E||, but marginally. The positive averaged E_n (cyan profiles, averaged over a 30 ms FPI-DES sampling period, in Figures 1b and 2b; see Figure 4Ad) before entering the current sheet represents the Hall electric field that points toward the current sheet (magenta arrows in Figure 3A). Its counterpart in the magnetosheath separatrix and/or exhaust region, i.e., negative E_n, is less clear in this event. A broader region with stronger Hall electric fields on the magnetospheric side than the magnetosheath side (to counter balance the magnetosheath pressure) has been predicted by PIC simulations for asymmetric reconnection [*Pritchett*, 2008; *Pritchett and Mozer*, 2009; *Chen et al*., 2016].

During the magenta-shade interval, the electron temperature shows a noticeable anisotropy, (magenta shade in Figures 1k and 2k) and bidirectional electrons on the magnetospheric side form pitch angle distributions enhanced at 0° and 180° (Figures 1, 2n, and 2o). During the yellow-shade period, an asymmetry between the 0° and 180° pitch angle electrons appears and later a combination of more field-aligned midenergy electrons and antiparallel low-energy populations is seen (Figures 1, 2n, and 2o). The symmetry near the separatrix region (magenta shade) indicates that inflowing electrons entering toward the Hall region are reflected and trapped by either an electrostatic potential or a mirror force associated with a decreasing magnetic strength near the central reconnection site [*Egedal et al*., 2005, 2008, 2013]. The observation at the edges of the exhaust region (yellow shades) is consistent with field-aligned fields/potentials accelerating electrons inward (toward the X line), combined with Fermi acceleration occurring in the exhaust region [*Drake et al*., 2009; *Lavraud et al*., 2016]. Toward the current sheet (0909:57.5–57.8 UT for MMS3 and 0909:57.95–58.25 UT for MMS4), low-energy (midenergy) electrons stream antiparallel (parallel) to the magnetic field. This indicates outward flowing magnetosheath electrons from the X line and inward acceleration of magnetospheric electrons by the field-aligned electric fields/potentials.

Bulk ion and electron velocities in the negative **l** ($V_{i,\,l} \approx -125$ km/s and $V_{e,\,l} \approx -480$ km/s in the current sheet or X line rest frame) increase at the current sheet (Figures 1, 2d, and 2e). This outflow jet, together with the positive B_n during the positive-to-negative B_l reversal, indicates a spacecraft crossing of the exhaust region south of a reconnection X line. $V_{i,\,l}$ in the current-sheet frame switches sign from negative to positive at ~0909:58.4

UT (MMS3; a blue arrow in Figure 1d) and ~0909:58.9 UT (MMS4; a blue arrow in Figure 2d). Almost simultaneously, B_m changes to the opposite polarity (negative to positive) Hall field (blue arrows in Figures 1a and 2a). This indicates that a reconnection X line moved southward (mostly along $-\mathbf{l}$), or alternatively, that the spacecraft moved northward past the vicinity of the X line.

Figure 3A depicts the spacecraft trajectory relative to the X line. The distance (x) of the spacecraft crossing the current sheet in the downstream (±**l**) direction from the X line can be estimated using the multispacecraft timing-induced current sheet and X line velocities ($v_{\mathrm{X\ line}}$) and symmetric reconnection geometry [*Phan et al.*, 2007]: $x = \Delta t_{\mathrm{mph}} v_{\mathrm{X\text{-}line},l}\left(\frac{\Delta t_{\mathrm{mph}}+\Delta t_{\mathrm{msh}}}{\Delta t_{\mathrm{mph}}-\Delta t_{\mathrm{msh}}}+1\right)$ where $\Delta t_{\mathrm{mph}}(\Delta t_{\mathrm{msh}})$ represents the duration of the MMS passage between the magnetospheric (magnetosheath) separatrix and the current sheet. The roughly estimated (due to the assumption of a symmetric reconnection geometry) distance, x, is ~4.2 d_i (the ion inertial length on the magnetosheath side, $d_i \approx 50$ km), which is incorporated in Figure 3A.

Around the current sheet crossing (blue shading in Figures 1 and 2f), the perpendicular electron jet velocity (blue profiles) in the $-\mathbf{l}$ direction is different from and faster than the $\mathbf{E}\times\mathbf{B}$ drift velocity calculated from the local electric and magnetic fields (black). When considering the uncertainly of $\mathbf{E}$ ($\delta\mathbf{E}$) in the $\mathbf{E}\times\mathbf{B}$ velocity (black dashed curves in Figure 1 and 2f show $(\mathbf{E}\pm\delta\mathbf{E})\times\mathbf{B}/B^2$), the difference is quite evident (marginally acceptable) for MMS4 (MMS3). On the other hand, the velocity components in the **m** and **n** directions are relatively consistent with the $\mathbf{E}\times\mathbf{B}$ drift (Figures 1, 2g, and 2h). Ion velocities (red profiles in Figures 1 and 2f–2h) disagree with the drift motion. This indicates that the ions (and the electrons, to some extent) are decoupled from the magnetic field.

To further explore the MMS traversal of the IDR and/or EDR, we carried out ion and electron Walén tests in each corresponding deHoffmann-Teller frame (Figure 3B). The Walén relation identifies a current sheet boundary layer undergoing reconnection as a rotational discontinuity. We used the generalized formula for the relation, derived by *Scudder et al.* [1999], that includes the effect of pressure anisotropies. The upstream conditions are obtained from the data averaged between 0909:55.70 and 0909:55.75 UT before MMS entering the separatrix region. From 0909:57 to 0909:59 UT, the ions do not satisfy the Walén test exhibiting a slope close to 0. (A slope of 1 is expected for current sheets undergoing reconnection.). The electron Walén test shows a slope closer to 1 (~0.8) although a portion of the data points disagrees with the trend. This suggests that the spacecraft was mostly in the IDR where only electrons were magnetized but they were likely passing the edge of the EDR where both ions and electrons were demagnetized.

4. The Outer Electron Diffusion Region

Figure 3C exhibits 2-D cuts of 3-D electron distributions (integrated over ±11.25° from the cut) with a 30 ms time resolution at selected times, denoted by cyan vertical lines "a" to "e" in Figures 1, 2, and 3A. The left and middle columns show the electron distributions as a function of ($\mathbf{V}_{||}$, $\mathbf{V}_{\perp 1}$) and ($\mathbf{V}_{||}$, $\mathbf{V}_{\perp 2}$), respectively. Parallel and perpendicular directions are defined with respect to the local magnetic field (**B**). The two perpendicular directions are chosen to be perpendicular to **B** approximately along the ion bulk velocity (**V**), $\mathbf{V}_{\perp 1} = \mathbf{B}\times(\mathbf{V}\times\mathbf{B})$ and $\mathbf{V}_{\perp 2} = \mathbf{B}\times\mathbf{V}$. The right column displays a cut of the distribution in the perpendicular-to-**B** plane, i.e., to $\mathbf{V}_{\perp 2}$ versus $\mathbf{V}_{\perp 1}$ directions.

Figure 3Ca shows the superposition of a magnetosheath electron population shaped as a half shell or crescent (blue arrows) and magnetospheric populations accelerated parallel to **B** (red arrows) before MMS3 enters the neutral sheet. Going forward in time for the MMS4 observation (Figures 3Cb–3Ce), electrons close to the magnetospheric separatrix (Figure 3Cb) show a greater spread in $\mathbf{V}_{||}$ than $\mathbf{V}\perp$, i.e., a temperature anisotropy ($T_{e,||} > T_{e,\perp}$). The distribution is superposed upon counterstreaming electron components (red arrows). Near the center of the large-amplitude electric field region (Figure 3Cc) the electrons exhibit more isotropic distributions containing the inward moving accelerated magnetospheric populations (red arrows) together with the antiparallel streaming magnetosheath electrons (blue arrows), possibly outflowing from the X line after having being accelerated there. Within the yellow shading in Figures 1 and 2d where the $E_{||}$ is marginally present (section 3), the counterstreaming electron components (e.g., Figures 3Cb and 3Cc) are observed to be asymmetric around $\mathbf{V}_{||} = 0$. *Hwang et al.* [2013] pointed out that the imbalance between electron beam components flowing into and leaving from an X line in the separatrix region, or reflection of a fraction of the electrons initially entering toward an X line, could result in the asymmetry. In this event, the field-aligned (mostly antiparallel) electric fields/potentials (Figure 2d) may, in part, contribute to a more substantial population accelerated inward (toward the X line, here, moving parallel to the magnetic field). *Ergun et al*. [2016] showed that similar large-amplitude $E_{||}$ structures develop on the magnetosphere side of the current layer when cold (<10 eV) magnetospheric electrons are mixing with warm (~100 eV) magnetosheath electrons on freshly reconnected magnetic field lines. They used the kinetic Vlasov code to show net parallel electric fields and electron acceleration toward the X line.

A structure similar to that in Figure 3Ca is seen in Figure 3Cd distributions sampled prior to MMS4 entering the neutral sheet. The half shell or crescent-shaped magnetosheath populations shown in the ($\mathbf{V}_{||}$, $\mathbf{V}_{\perp 1}$) and ($\mathbf{V}_{||}$, $\mathbf{V}_{\perp 2}$) distributions (blue arrows) give rise to a certain level of agyrotropy, i.e., a lack of axisymmetry in the ($\mathbf{V}_{\perp 1}$, $\mathbf{V}_{\perp 2}$) distributions. Closer to the sheet (Figure 3Ce), a partial shell-like structure with a narrower opening angle and a smaller distance from the origin appears (blue arrows). Recent PIC simulations [*Chen et al*., 2016] predict that this unique crescent shape in the ($\mathbf{V}_{||}$, $\mathbf{V}_{\perp}$) distributions originates from accelerated meandering magnetosheath electrons (near the X line [*Hesse et al*., 2014; *Burch et al*., 2016]) that are then cyclotron turned by the reconnected magnetic field to produce the outflow jet downstream the X line. In particular, the predicted electron distribution at the outer edge of the EDR (at location "j5"—about $3d_i$ downstream from an X line—in Figure 2 of *Chen et al*. [2016]; as marked in Figure 4B) shows a striking agreement to Figures 3Ca and 3Cd. Furthermore, the distributions observed by MMS approaching the neutral sheet (Figure 3Ce) are similar to "j2" or "j3" in Figure 2 of the same paper that are sampled near the simulated neutral sheet. *Bessho et al*. [2016] analytically showed that the opening of the crescent shape in a distribution becomes wider, and the distance of the outer crescent periphery from the origin becomes larger farther away from the X line toward the stagnant point in the central reconnection region. Similarly, *Shay et al*. [2016] performed a PIC simulation to show that the parallel outflow crescent has the same peak velocity as the crescent around the X line. These studies explain the observation that the radius of the crescent shape and its opening from the origin become smaller as MMS approach the neutral sheet (Figures 3Cd and 3Ce).

We estimated current densities using particle data, $q(n_i v_i + n_e v_e)$, from MMS4 (Figure 4Ab). (The curlometer technique [*Dunlop et al*., 2002] cannot resolve the structure below scales comparable to the spacecraft separation, which is much larger than electron scales in this event.) Prior to crossing the neutral sheet (marked by the vertical magenta dashed line) where the peculiar crescent distributions appear and immediately after the current sheet crossing, the current density along l peaks at ~1100 nA/m^2 (cyan arrows in Figure 4Ab). This current is mainly carried by the electron jets outflowing from the X line, consistent with the strong jets downstream from the X line in the outer EDR, as predicted by the simulation (Figure 4Ba). Around the neutral sheet, negative J_m components associated with the magnetic field reversal become significant.

Hesse et al. [2008] reported that the electron flow jets are a combination of the $\mathbf{E}\times\mathbf{B}$ drift and of diamagnetic effects associated with the pressure gradients. Figures 4Ac and 4Ad show that the E_m and E_n components (black profiles) are balanced mainly by the convective bulk electron inertial term, $-\mathbf{V}_e\times\mathbf{B}$ (blue profiles). Differences between the two (cyan arrows in Figures 4Ac and 4Ad) suggest a certain contribution from the pressure tensor gradient term, $-(\nabla\cdot\leftrightarrow\mathrm{P}_\mathbf{e})/ne$. (Neither four-spacecraft nor single-spacecraft calculations suffice to estimate $-(\nabla\cdot\leftrightarrow\mathrm{P}_\mathbf{e})/ne$ for this event due to the relatively large spacecraft separation and nonstationary structure.) The current-sheet normal electric field (E_n) is mostly positive (negative) before (after) crossing the current sheet, i.e., pointing toward the current sheet and stronger on the magnetospheric side (Figure 4Ad). This asymmetric electric field also features in the simulation and extends to the outer EDR and along the magnetospheric separatrices, consistent with Figure 4Bb.

The bursty electric field in the magnetosphere side of the current layer in this event leads to large fluctuations in the electric field in the electron frame, $\mathbf{E}' = \mathbf{E} + \mathbf{V}_e\times\mathbf{B}$ (Figure 4Ae). The nonzero electric field in the electron frame has been used as an indicator of the violation of the ideal frozen-in condition, although it is not sufficient for the identification of the EDR [e.g., *Zenitani et al*., 2011]. We note that the out-of-plane component of $\mathbf{E}'\left(E'_m\right)$ is positive during the current sheet crossing (magenta shading in Figure 4Ae), which is opposite to the presumed reconnection electric field (negative E'_m) near the central current sheet. Accordingly, the Joule heating, or the electron dissipation measure following *Zenitani et al*. [2011], $\mathbf{J}\cdot\mathbf{E}'$ is negative (magenta shading in Figure 4Af). These observations further support the case for MMS encountering the outer EDR, where the electron jets outrun the moving magnetic field (blue shading in Figure 2f), leading to E'_m having an opposite sign to the inner-EDR E'_m and $\mathbf{J} \cdot \mathbf{E}' < 0$. Both features well agree with the PIC predictions shown in Figures 4Bc and 4Bd.

Karimabadi et al. [2007] showed that at the edge of the EDR the electron jets slow down, converting the bulk kinetic energy to thermal energy. We investigate the energy transfer occurring at the outer EDR for the present event by plotting $\mathbf{V}_e \cdot (\mathbf{J} \times \mathbf{B})$, indicating energy transfer between the magnetic and bulk kinetic energy (blue profiles in Figure 4Af) [*Birn and Hesse*, 2010]. Comparing with the Joule heating term $\mathbf{J} \cdot \mathbf{E}'$ (black), we find a rough relationship indicating that $\mathbf{J} \cdot \mathbf{E}'$ is counter balanced by $\mathbf{V}_e \cdot (\mathbf{J} \times \mathbf{B})$ around the current sheet crossing except for an intermittent period between 0909:58.45 and 58.5 UT (marked by magenta shading in Figure 4Af). This indicates that the bulk kinetic energy is mostly transferred to the field energy.

5. Summary

The paper presents a case study of an asymmetric reconnection event observed on the postnoon magnetopause by the Magnetospheric Multiscale (MMS) mission. The high-resolution measurements of the electric/magnetic field and electron distributions enabled us to explore the fine structure of the diffusion region near the X line. The event features large-amplitude bursty electric fields near/inside the magnetospheric separatrix, ions decoupled from the magnetic field over the current sheet crossing, outflowing electron jets downstream of the X line at speeds greater than the $\mathbf{E} \times \mathbf{B}$ drift velocity, and crescent-shaped electron distributions focused along $\mathbf{V}_{||}$ prior to entering the current sheet.

The net field-aligned components in the electric field may accelerate electrons along **B**, resulting in $T_{e,||} > T_{e,\perp}$. Toward the current sheet, a superposition of outward flowing magnetosheath electrons from the X line and magnetospheric electrons accelerated inward by the field-aligned electric fields/potentials appears in the particle distributions. The partial shell-like or crescent distributions are observed in close proximity to the current sheet, where the out-of-plane electric field exhibits an opposite polarity to the reconnection electric field, and the energy is converted from bulk kinetic to field energy. These observations show excellent agreement with the properties of the outer EDR downstream of the model reconnection X line [*Chen et al*., 2016]. Therefore, we suggest interpreting this event as an MMS passage through the edge of the elongated EDR or the outer EDR in the exhaust region.

Acknowledgments
This study was supported, in part, by NASA's MMS project at the Goddard Space Flight Center, NSF AGS-1305374 and AGS-1602510, NASA NNX16AI39G, and ISSI program: MMS and Cluster observations of magnetic reconnection (team members are N. Aunai, J. Dargent, J. Eastwood, P. Escoubet, R. Fear, H. Fu, K.-J. Hwang, Y. Khotyaintsev, G. Lapenta, B. Lavraud, C. Norgren, D. Sibeck, S. Toledo-Redondo, and A. Varsani). MMS data sets were provided by the MMS science working group teams through the link (http//lasp.colorado.edu/mms/sdc/public/). We acknowledge MMS FPI (Thomas E. Moore, Yoshifumi Saito, Jean-Andre Sauvaud, Victoria Coffey, Benoit Lavraud, Michael Chandler, and Conrad Schiff) and Field teams for providing data. K.J.H. thanks Li-Jen Chen for providing the result of PIC simulations and Naoki Bessho for a useful personal conversation, and all the members of the MMS instruments and Modeling/Theory team.

References

Bessho, N., L.-J. Chen, J. R. Shuster, and S. Wang (2014), Electron distribution functions in the electron diffusion region of magnetic reconnection: Physics behind the fine structures, *Geophys. Res. Lett.*, *41*, 8688–8695, doi:10.1002/2014GL062034.

Bessho, N., L.-J. Chen, and M. Hesse (2016), Electron distribution functions in the diffusion region of asymmetric magnetic reconnection, *Geophys. Res. Lett.*, *43*, 1828–1836, doi:10.1002/2016GL067886.

Birn, J., and M. Hesse (2010), Energy release and transfer in guide field reconnection, *Phys. Plasmas*, *17*, 012,109.

Birn, J., et al. (2001), Geospace environmental modeling gem magnetic reconnection, *J. Geophys. Res.*, *106*, 3715–3719, doi:10.1029/1999JA900449.

Burch, J. L., T. E. Moore, R. B. Torbert, and B. L. Giles (2015), Magnetospheric multiscale overview and science objectives, *Space Sci. Rev.*, 1–17, doi:10.1007/s11214-015-0164-9.

Burch, J. L., et al. (2016), Electron-scale measurements of magnetic reconnection in space, *Science*, *352*(6290), doi:10.1126/science.aaf2939.

Chen, L.-J., M. Hesse, S. Wang, N. Bessho, and W. Daughton (2016), Electron energization and structure of the diffusion region during asymmetric reconnection, *Geophys. Res. Lett.*, *43*, 2405–2412, doi:10.1002/2016GL068243.

Daughton, W., J. Scudder, and H. Karimabadi (2006), Fully kinetic simulations of undriven magnetic reconnection with open boundary conditions, *Phys. Plasmas*, *13*(7), 072101.

Drake, J. F., M. Swisdak, T. D. Phan, P. A. Cassak, M. A. Shay, S. T. Lepri, R. P. Lin, E. Quataert, and T. H. Zurbuchen (2009), Ion heating resulting from pickup in magnetic reconnection exhausts, *J. Geophys. Res.*, *114*, A05111, doi:10.1029/2008JA013701.

Dunlop, M., A. Balogh, K.-H. Glassmeier, and P. Robert (2002), Four-point Cluster application of magnetic field analysis tools: The curlometer, *J. Geophys. Res.*, *107*(A11), 1384, doi:10.1029/2001JA005088.

Egedal, J., M. Øieroset, W. Fox, and R. P. Lin (2005), In situ discovery of an electrostatic potential, trapping electrons and mediating fast reconnection in the Earth's magnetotail, *Phys. Rev. Lett.*, *94*, 025006, doi:10.1029/2009JA014650.

Egedal, J., W. Fox, M. Porkolab, M. Øieroset, R. P. Lin, W. Daughton, and J. F. Drake (2008), Evidence and theory for trapped electrons in guide field magnetotail reconnection, *J. Geophys. Res.*, *113*, A12207, doi:10.1029/2008JA013520.

Egedal, J., W. Daughton, and A. Le (2012), Large-scale electron acceleration by parallel electric fields during magnetic reconnection, *Nat. Phys.*, *8*, 321–324, doi:10.1038/nphys2249.

Egedal, J., A. Le, and W. Daughton (2013), A review of pressure anisotropy caused by electron trapping in collisionless plasma, and its implications for magnetic reconnection, *Phys. Plasmas*, *20*, 18, doi:10.1063/1.4811092.

Engwall, E., A. I. Eriksson, M. André, I. Dandouras, G. Paschmann, J. Quinn, and K. Torkar (2006), Low-energy (order 10 eV) ion flow in the magnetotail lobes inferred from spacecraft wake observations, *Geophys. Res. Lett.*, *33*, L06110, doi:10.1029/2005GL025179.

Ergun, R. E., et al. (2014), The axial double probe and fields signal processing for the MMS mission, *Space Sci. Rev.*, 1–22, doi:10.1007/s11214-014-0115-x.

Ergun, R. E., et al. (2016), Magnetospheric Multiscale observations of large-amplitude, parallel, electrostatic waves associated with magnetic reconnection at the magnetopause, *Geophys. Res. Lett.*, *43*, 5626–5634, doi:10.1002/2016GL068992.

Eriksson, S., et al. (2016), Magnetospheric Multiscale observations of the electron diffusion region of large guide field magnetic reconnection, *Phys. Rev. Lett.*, *117*, 015001, doi:10.1103/PhysRevLett.117.015001.

Fujimoto, K. (2006), Time evolution of the electron diffusion region and the reconnection rate in fully kinetic and large system, *Phys. Plasmas*, *13*, 072,904.

Gosling, J. T., M. F. Thomsen, S. J. Bame, R. C. Elphic, and C. T. Russell (1990), Cold ion beams in the low latitude boundary layer during accelerated flow events, *Geophys. Res. Lett.*, *17*, 2245–2248, doi:10.1029/GL017i012p02245.

Hesse, M. (2006), Dissipation in magnetic reconnection with a guide magnetic field, *Phys. Plasmas*, *13*, 122107.

Hesse, M., K. Shindler, J. Birn, and M. Kuznetsova (1999), The diffusion region in collisionless magnetic reconnection, *Phys. Plasmas*, *5*, 1781.

Hesse, M., S. Zenitani, and A. Klimas (2008), The structure of the electron outflow jet in collisionless magnetic reconnection plasma, *Phys. Plasmas*, *15*, 112,102.

Hesse, M., N. Aunai, D. Sibeck, and J. Birn (2014), On the electron diffusion region in planar, asymmetric, systems, *Geophys. Res. Lett.*, *41*, 8673–8680, doi:10.1002/2014GL061586.

Hwang, K.-J., M. L. Goldstein, D. E. Wendel, A. N. Fazakerley, and C. Gurgiolo (2013), Cluster observations near reconnection X-lines in Earth's magnetotail current sheet, *J. Geophys. Res. Space Physics*, *118*, 4199–4209, doi:10.1002/jgra.50403.

Karimabadi, H., W. Daughton, and J. Scudder (2007), Multi-scale structure of the electron diffusion region, *Geophys. Res. Lett.*, *34*, L13104, doi:10.1029/2007GL030306.

Khotyaintsev, Y. V., et al. (2016), Electron jet of asymmetric reconnection, *Geophys. Res. Lett.*, *43*, 5571–5580, doi:10.1002/2016GL069064.

Lavraud, B., et al. (2016), Currents and associated electron scattering and bouncing near the diffusion region at Earth's magnetopause, *Geophys. Res. Lett.*, *43*, 3042–3050, doi:10.1002/2016GL068359.

Lepping, R. P., and K. W. Behannon (1980), Magnetic field directional discontinuities: 1. Minimum variance errors, *J. Geophys. Res.*, *85*, 4695–4703, doi:10.1029/JA085iA09p04695.

Lindqvist, P.-A., et al. (2016), The spin-plane double probe electric field instrument for MMS, *Space Sci. Rev.*, *199*(1-4), 137–165.

Mozer, F. S., V. Angelopoulos, J. Bonnell, K. H. Glassmeier, and J. P. McFadden (2008), THEMIS observations of modified Hall fields in asymmetric magnetic field reconnection, *Geophys. Res. Lett.*, *35*, L17S04, doi:10.1029/2007GL033033.

Nakamura, T. K. M., M. Fujimoto, and A. Otto (2006), Magnetic reconnection induced by weak Kelvin-Helmholtz instability and the formation of the low-latitude boundary layer, *Geophys. Res. Lett.*, *33*, L14106, doi:10.1029/2006GL026318.

Norgren, C., et al. (2016), Finite gyroradius effects in the electron outflow of asymmetric magnetic reconnection, *Geophys. Res. Lett.*, *43*, 6724–6733, doi:10.1002/2016GL069205.

Otto, A., and D. H. Fairfield (2000), Kelvin-Helmholtz instability at the magnetotail boundary: MHD simulation and comparison with Geotail observations, *J. Geophys. Res.*, *105*, 21,175–21,190, doi:10.1029/1999JA000312.

Paschmann, G., and P. W. Daly (1998), Analysis methods for multispacecraft data, Sci. Rep. 001, Int. Space Sci. Inst., Bern.

Phan, T. D., J. F. Drake, M. A. Shay, F. S. Mozer, and J. P. Eastwood (2007), Evidence for an elongated (>60 ion skin depths) electron diffusion region during fast magnetic reconnection, *Phys. Rev. Lett.*, *99*, 225002.

Pollock, C., et al. (2016), Fast Plasma Investigation for Magnetospheric Multiscale, *Space Sci. Rev.*, doi:10.1007/s11214-016-0245-4.

Pritchett, P. L. (2008), Collisionless magnetic reconnection in an asymmetric current sheet, *J. Geophys. Res.*, *113*, A06210, doi:10.1029/2007JA012930.

Pritchett, P. L., and F. S. Mozer (2009), Asymmetric magnetic reconnection in the presence of a guide field, *J. Geophys. Res.*, *114*, A11210, doi:10.1029/2009JA014343.

Ricci, P., G. Lapenta, and J. U. Brackbill (2002), Gem reconnection challenge: Implicit kinetic simulations with the physical mass ratio, *Geophys. Res. Lett.*, *29*(23), 2088, doi:10.1029/2002GL015314.

Rogers, B. N., R. E. Denton, J. F. Drake, and M. A. Shay (2001), Role of dispersive waves in collisionless magnetic reconnection, *Phys. Rev. Lett.*, *87*, 195,004.

Russell, C. T., et al (2014), The Magnetospheric Multiscale magnetometers, *Space Sci. Rev.*, doi:10.1007/s11214-014-0057-3.

Scudder, J. D., P. A. Puhl-Quinn, F. S. Mozer, K. W. Ogilvie, and C. T. Russell (1999), Generalized Walén tests through Alfvén waves and rotational discontinuities using electron flow velocities, *J. Geophys. Res.*, *104*, 19,817–19,834, doi:10.1029/1999JA900146.

Sonnerup, B. U. Ö, and M. Scheible (1998), Minimum and maximum variance analysis, in *Analysis Methods for Multi-Spacecraft Data*, edited by G. Paschmann and P. W. Daly, pp. 185–220, Int. Space Sci. Inst., Bern.

Shay, A., J. F. Drake, and M. Swisdak (2007), Two-scale structure of the electron dissipation region during collisionless magnetic reconnection, *Phys. Rev. Lett.*, *99*, 155002.

Shay, M. A., J. F. Drake, M. B. N. Rogers, and R. E. Denton (2001), Alfvénic collisionless magnetic reconnection and the Hall term, *J. Geophys. Res.*, *106*, 3759–3772, doi:10.1029/1999JA001007.

Shay, M. A., T. D. Phan, C. C. Haggerty, M. Fujimoto, J. F. Drake, K. Malakit, P. A. Cassak, and M. Swisdak (2016), Kinetic signatures of the region surrounding the X line in asymmetric (magnetopause) reconnection, *Geophys. Res. Lett.*, *43*, 4145–4154, doi:10.1002/2016GL069034.

Shuster, J. R., L.-J. Chen, M. Hesse, M. R. Argall, W. Daughton, R. B. Torbert, and N. Bessho (2015), Spatiotemporal evolution of electron characteristics in the electron diffusion region of magnetic reconnection: Implications for acceleration and heating, *Geophys. Res. Lett.*, *42*, 2586–2593, doi:10.1002/2015GL063601.

Zenitani, S., M. Hesse, A. Klimas, and M. Kuznetsova (2011), New measure of the diffusion region in collisionless magnetic reconnection, *Phys. Rev. Lett.*, *106*, 195003.